Journal of Colloid and Interface Science 718 (2026) 140469

Contents lists available at ScienceDirect

Journal of Colloid And Interface Science

journal homepage: www.elsevier.com/locate/jcis

Metal-free frustrated Lewis pairs on boron-doped nitrogen-deficient carbon nitride boosting photocatalytic hydrogen peroxide generation

Lei Li [a,1], Hangjing Yu [a,1], Kangjie Gao [b], Linfeng Jin [c,*], Jinyang Zhang [d], Wentao Wang [d,*], Yong Hu [b,*]

[a] *Key Laboratory of the Ministry of Education for Advanced Catalysis Materials, Department of Chemistry, Zhejiang Normal University, Jinhua 321004, China*
[b] *Institute of Nanocatalysis and Energy Conversion, College of Chemistry and Materials Engineering, Zhejiang A&F University, Hangzhou 311300, China*
[c] *Department of Physics, College of Physics and Electronic Information Engineering, Zhejiang Normal University, Jinhua 321004, China*
[d] *Guizhou Provincial Key Laboratory of Computational Nano-Material Science, Guizhou Education University, Guiyang 550018, China.*

HIGHLIGHTS

- The metal-free FLPs within g-C_3N_4 via a one-step boronization treatment.
- The tailored FLPs boost exciton dissociation and reduce the exciton binding energy.
- The "push-pull" effect can promote O_2 activation and suppress the O–O bond cleavage.
- BNDCN photocatalyst steers the two-electron ORR toward selective H_2O_2 production.

GRAPHICAL ABSTRACT

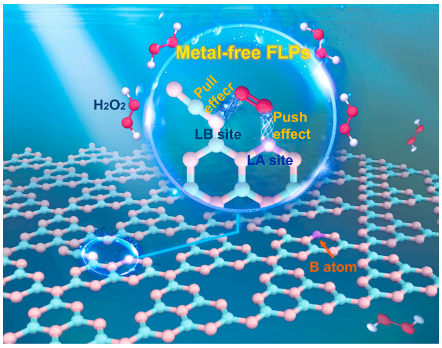

ARTICLE INFO

Keywords:
Carbon nitrides
Boron dopant
Nitrogen deficiency
Frustrated Lewis pairs
H_2O_2 photoproduction

ABSTRACT

Developing efficient metal-free catalysts for the selective two-electron photoreduction of O_2 to H_2O_2 remains a formidable challenge in photocatalysis. Herein, we report a strategy to address this by engineering atomically dispersed frustrated Lewis pairs (FLPs) into boron-doped nitrogen-deficient carbon nitride (BNDCN). Structural analyses unambiguously identify electron-deficient boron and adjacent cyano-group nitrogen as complementary Lewis acid and base sites, forming well-defined FLP configurations. The optimized BNDCN catalyst achieves a remarkable H_2O_2 production rate of 11.3 mmol g^{-1} h^{-1} with an apparent quantum efficiency of 13.1% at 420 nm, ranking it among the best-performing metal-free photocatalysts. Moreover, the photocatalytic reaction solution exhibits significant antibacterial activity, underscoring its potential for practical applications. Combined mechanistic studies reveal that the tailored FLPs generate a strongly polarized local field that promotes exciton dissociation, reduces the exciton binding energy, and significantly enhances charge separation and transfer. The induced "push-pull" electronic effect simultaneously facilitates O_2 adsorption, stabilizes critical *OOH intermediates, and suppresses the O—O bond cleavage, thereby exclusively steering the reaction along the two-electron reduction pathway. This work pioneers a design paradigm for constructing metal-free FLP

---

[*] Corresponding authors.
E-mail addresses: jlf@zjnu.cn (L. Jin), wtwang@gznc.edu.cn (W. Wang), yonghu@zafu.edu.cn, yonghu@zjnu.edu.cn (Y. Hu).
[1] These authors contributed equally to this work.

https://doi.org/10.1016/j.jcis.2026.140469
Received 3 February 2026; Received in revised form 22 March 2026; Accepted 5 April 2026

photocatalysts, elucidates the pivotal role of local polarization in molecular activation, and offers fundamental insights for solar-driven chemical conversion.

1. Introduction

Hydrogen peroxide (H_2O_2) is a mild and environmentally benign oxidant with extensive applications across the chemical industry, energy storage, disinfection, and wastewater treatment [1]. Its current industrial production, however, predominantly relies on the anthraquinone oxidation process, which involves energy-intensive steps, complex operations, and the generation of hazardous waste [2,3]. Therefore, the development of green and sustainable synthesis routes to H_2O_2 is of great urgency. Among the emerging alternatives, photocatalytic oxygen reduction (O_2PR) has garnered significant interest as a promising strategy, leveraging clean solar energy, environmentally friendly reactants, and cost-effective photocatalysts [4,5]. Notably, the efficiency of H_2O_2 production via O_2PR hinges critically on the rational design and synthesis of advanced photocatalysts.

Engineering photocatalysts through strategies such as cocatalyst loading [6], hetero-atom doping [7,8], incorporation of organic functional groups [9,10], or modification with inorganic bases [11,12] has been shown to enhance O_2 adsorption and activation. In these systems, catalytic sites serve as a crucial medium, simultaneously mediating charge transfer and molecular activation. Depending on their configuration, O_2 adsorption on catalysts generally follows two primary modes: Pauling-type adsorption at a single site and Yeager-type adsorption at dual sites [9]. In Pauling adsorption, monodentate anchoring via a single O atom, particularly at metal active site, induces spatial asymmetry in the orbital coupling between O_2 and the catalyst (**Scheme 1**a) [13,14]. This anisotropic configuration restricts charge transfer to a unidirectional pathway through the adsorbed O atom and may lead to orbital decoupling within the O—O bonds of the adsorbed oxygen species ($^*O_2$) and hydroperoxyl radical (·OOH) intermediates. As a result, both the activity and selectivity of the two-electron ($2e^-$) O_2PR toward H_2O_2 are often compromised. Theoretically, weakening the electronic interaction between the active site and $^*O_2$/·OOH intermediate can suppress O—O bond cleavage, favoring the $2e^-$ pathway over the four-electron ($4e^-$) reduction to H_2O. Nevertheless, the monodentate O-anchoring configuration alone is typically insufficient to achieve both effective O_2 adsorption/activation and concurrent suppression of O—O bond cleavage in the key $^*O_2$/·OOH intermediate.

Recently, frustrated Lewis pairs (FLPs) have emerged as a promising Yeager-type adsorption configuration for the selective activation of O_2. Comprising sterically hindered electron-deficient Lewis acid (LA) and electron-rich Lewis base (LB) sites [15,16], FLPs can effectively activate O_2 molecule while suppressing cleavage of the O—O bond. Upon interaction with O_2, electrons are transferred from O_2 bonding orbitals to the vacant orbitals of the LA, while the LB concurrently donates electrons into O_2 antibonding orbitals [17,18], creating a cooperative "push−pull" effect that facilitates both O_2 activation and reaction kinetics. In contrast, conventional dual-metal-site catalysts often exhibit excessively strong electronic interaction with O_2, which can overweaken or even cleave the O—O bond, thereby favoring the $4e^-$ reduction to H_2O over the selective $2e^-$ pathway to H_2O_2 (**Scheme 1**b) [19,20]. These considerations underscore the need to develop dual-site catalysts with moderated O_2 coupling strength, balancing activation capability with charge-transfer efficiency to steer the reaction selectively toward the $2e^-$ O_2PR.

Given that graphitic carbon nitride (CN) features abundant electron-rich N atoms, introducing electron-deficient B atoms can generate metal-free FLPs within the CN framework, offering potential for efficient

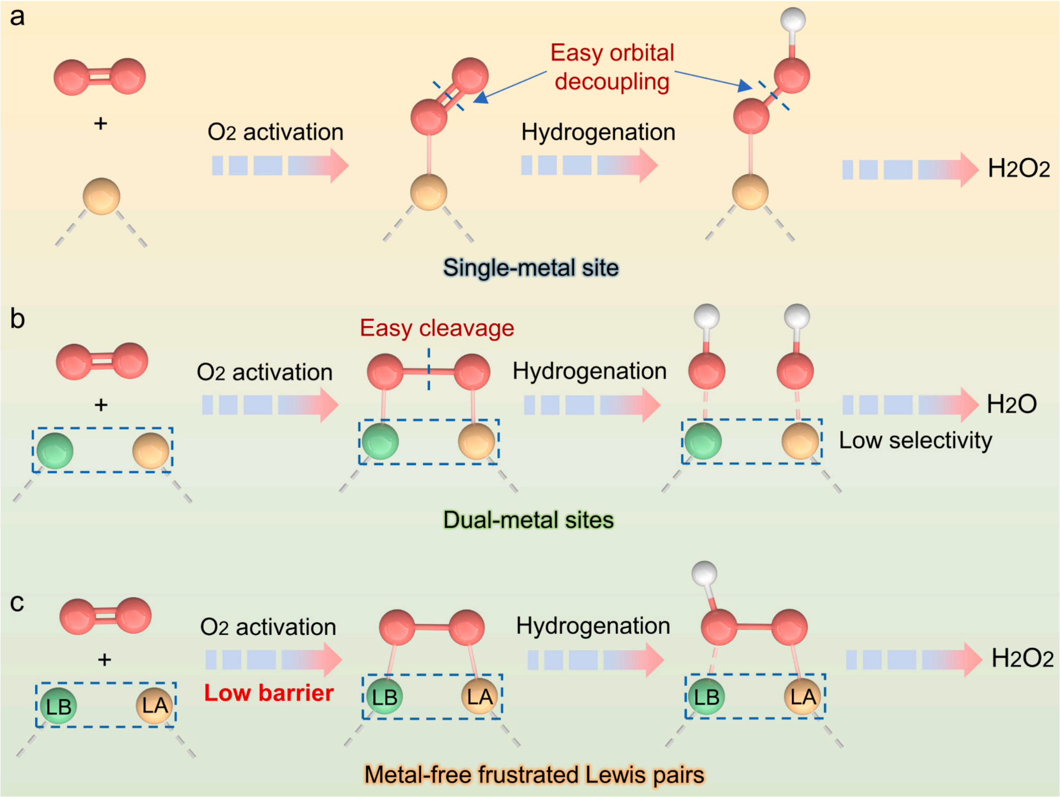

Scheme 1. Photoreduction of O_2 into H_2O_2 or H_2O on (a) a single-metal site, (b) dual-metal sites, and (c) metal-free FLPs.

photocatalytic H_2O_2 synthesis from O_2 [21,22]. Owing to this unique configuration, the atomically dispersed metal-free FLPs provide a stable polarized environment and exhibit high reactivity, selectivity, active-site utilization, and structural stability, all of which favor O_2 activation and enhance photocatalytic activity (**Scheme 1**c). Nevertheless, constructing such atomically dispersed metal-free FLP sites and elucidating their catalytic mechanism remain significant challenges.

Guided by these insights, we constructed atomically dispersed metal-free FLPs within CN via a one-step boronization treatment under an inert atmosphere, aiming to achieve efficient photocatalytic H_2O_2 production. Experimental and theoretical analyses reveal that the resulting boron-doped and nitrogen-defect-engineered CN (denoted as BNDCN) features electron-deficient B atoms as Lewis acid (LA) sites and electron-rich N atoms adjacent to cyan groups as Lewis base (LB) sites, together forming a well-defined metal-free FLP structure. Mechanistic studies further demonstrate that the distinctive "push–pull" electronic effect within these metal-free FLPs promotes efficient O_2 activation, significantly enhancing both the activity and selectivity of the $2e^-$ O_2PR pathway toward H_2O_2 formation. As a result, the optimized BNDCN catalyst exhibits substantially enhanced O_2PR performance, yielding H_2O_2 production rates of 11.3 mmol g^{-1} h^{-1} and 628 μmol g^{-1} h^{-1} with and without a sacrificial agent, respectively. These rates are approximately 6.3 and 9.7 times higher than those of CN nanosheets (NSs) (1.8 mmol g^{-1} h^{-1} and 65 μmol g^{-1} h^{-1}, respectively). Besides, the photocatalytic reaction solution displays excellent sterilization efficacy. This work offers valuable guidance for the rational design of high-efficiency metal-free FLPs in photocatalysts for the O_2PR, thereby advancing the fundamental understanding of their role in O_2 activation.

2. Experimental section

2.1. Materials

Analytical-grade melamine, $NaBH_4$, NaCl, anhydrous sodium sulfate (Na_2SO_4), potassium iodide (KI), ammonium molybdate ($(NH_4)_6Mo_7O_{24}$), and isopropyl alcohol were purchased from Sinopharm Chemical Reagent Co., Ltd. (China) and directly used without further purification. Analytical-grade 5, 5-dimethyl-1-pyrroline-N -oxide (DMPO) and 2, 2, 6, 6-tetramethyl-4-piperidone hydrochloride (TEMP) agent were purchased from Aladdin Chemical Reagent Co., Ltd. (China) and directly used without further purification. Deionized water was used throughout the work.

2.2. Synthesis of CN NSs

Typically, 2000 mg of melamine in a covered porcelain crucible was wrapped in tin foil and calcined at 520 °C in air atmosphere for 4 h with a ramping rate of 5 °C min^{-1}. The obtained bulk CN was collected and ground into a powder. 1000 mg of bulk CN was calcined again using the same conditions to obtain CN NSs.

2.3. Synthesis of BNDCN

In detail, 200 mg of CN NSs and various amounts of $NaBH_4$ (20, 40, 60, and 80 mg) were finely ground and then calcined at 400 °C in a N_2 atmosphere for 1 h with a ramping rate of 10 °C min^{-1}. The obtained products were washed several times using deionized water to remove unreacted $NaBH_4$. The product was finally obtained through freeze-drying. The obtained samples were denoted as BNDCN–X (X = 1–4).

2.4. Synthesis of NDCN

The NDCN was obtained using the same method as the preparation of BNDCN–3 sample except that NaCl replaced $NaBH_4$.

Other experimental details, including material characterizations, O_2PR, photophysical and (photo)electrochemical measurements, and theoretical calculations, can be found in the Supporting Information.

3. Results and discussion

3.1. Chemical structure characterization

The synthesis of BNDCN involved a multi-step calcination process (**Fig. 1**a). First, bulk CN was obtained through the thermal polymerization of melamine, which was then thermally exfoliated to produce CN NSs. Subsequently, the CN NSs were subjected to thermal treatment with different loadings of $NaBH_4$ to yield the target BNDCN catalysts [23]. These samples were then evaluated as photocatalysts for H_2O_2 evolution studies. Field-emission scanning electron microscopy (FESEM) images show that bulk CN consists of micrometer-sized particles (**Fig. S1**). In contrast, the exfoliated CN, nitrogen-deficient CN (NDCN), and all BNDCN display a similar sheet-like structure on the micrometer scale (**Fig. S2**). Transmission electron microscopy (TEM) image of the BNDCN–3 further confirms the porous morphology, showing pores with sizes ranging from tens to hundreds of nanometers (outlined by orange lines in **Fig. 1**b). High-resolution TEM (HRTEM) analysis indicates a sheet-like morphology at the microscopic scale (**Fig. 1**c). Furthermore, elemental mapping confirms the homogeneous distribution of C, N, and B elements throughout the BNDCN–3 (**Fig. S3**).

The powder X-ray diffraction (XRD) patterns of all as-prepared samples exhibit two characteristic diffraction peaks of the CN phase at 12.9° and 27.4°, corresponding to the (100) plane of in-plane repeating heptazine units and the (002) plane of interlayer stacking of conjugated aromatic structures, respectively (**Fig. S4**a) [24,25]. Notably, the (100) and (002) diffraction peaks of BNDCN gradually weaken and broaden, indicating a disruption of the long-range atomic order following $NaBH_4$ thermal treatment [26]. Moreover, the enlarged (100) diffraction peak of BNDCN shifts noticeably toward lower diffraction angles relative to those of CN and NDCN, primarily due to the substitution of C atoms by B dopants (**Fig. S4**b) [23]. Fourier transform infrared spectroscopy (FTIR) analyses of BNDCN and control samples display similar characteristic bands (**Fig. 1**d). The absorption band at 803 cm^{-1} is assigned to the breathing mode of *s*-triazine units, while those between 1200 and 1700 cm^{-1} correspond to the stretching vibrations of aromatic C—N heterocycles [27]. The broad absorption band at 3000–3500 cm^{-1} is attributed to the N−H stretching vibrations. A new absorption band at 2180 cm^{-1}, present in NDCN and BNDCN, is ascribed to cyano group (nitrogen defect) [28], indicating the partial opening of the *s*-triazine heterocycles upon defect formation. Additionally, nitrogen adsorption–desorption isotherms show that the CN, NDCN, and BNDCN–3 samples have comparable specific surface areas and similar mesoporous structure (**Fig. S5**), which ensures a high density of accessible active sites.

X-ray photoelectron spectroscopy (XPS) analysis was conducted to elucidate the defect states and chemical compositions of the as-prepared catalysts. The survey XPS and elemental compositions unveil the presence of C, N, B, and physically adsorbed Na elements in the BNDCN–3 catalyst (**Fig. S6**a, **Tables S1-S4**). The C 1 s XPS spectrum of CN displays two characteristic peaks at 284.80 and 288.44 eV, corresponding to adventitious carbon and N–C=N in the aromatic rings, respectively (**Fig. 1**e) [29]. The N 1 s spectrum can be deconvolved into three peaks at 398.82, 399.58, and 400.89 eV, assigned to the C–N=C, N–$(C)_3$, and –NH&NH_2 groups within the heptazine framework, respectively (**Fig. S6**b) [30]. A new peak emerges at 286.70 eV in the C 1 s XPS spectrum of NDCN, attributed to the cyano group (**Fig. 1**e) [28]. Compared to those of CN, NDCN exhibits slightly lower binding energies for the C–N=C species in both C 1 s and N 1 s spectra, indicating that the introduction of cyano group enhances the electron density around N and C atoms (**Figs. 1**e and **S6**b). Notably, the BNDCN–3 sample exhibits further decreased binding energies for both the C–N=C and the cyano group compared to NDCN. This shift can be ascribed to the incorporation of B atoms with lower electronegativity and their synergistic interaction with the cyano group [31]. Furthermore, the B 1 s high-resolution XPS

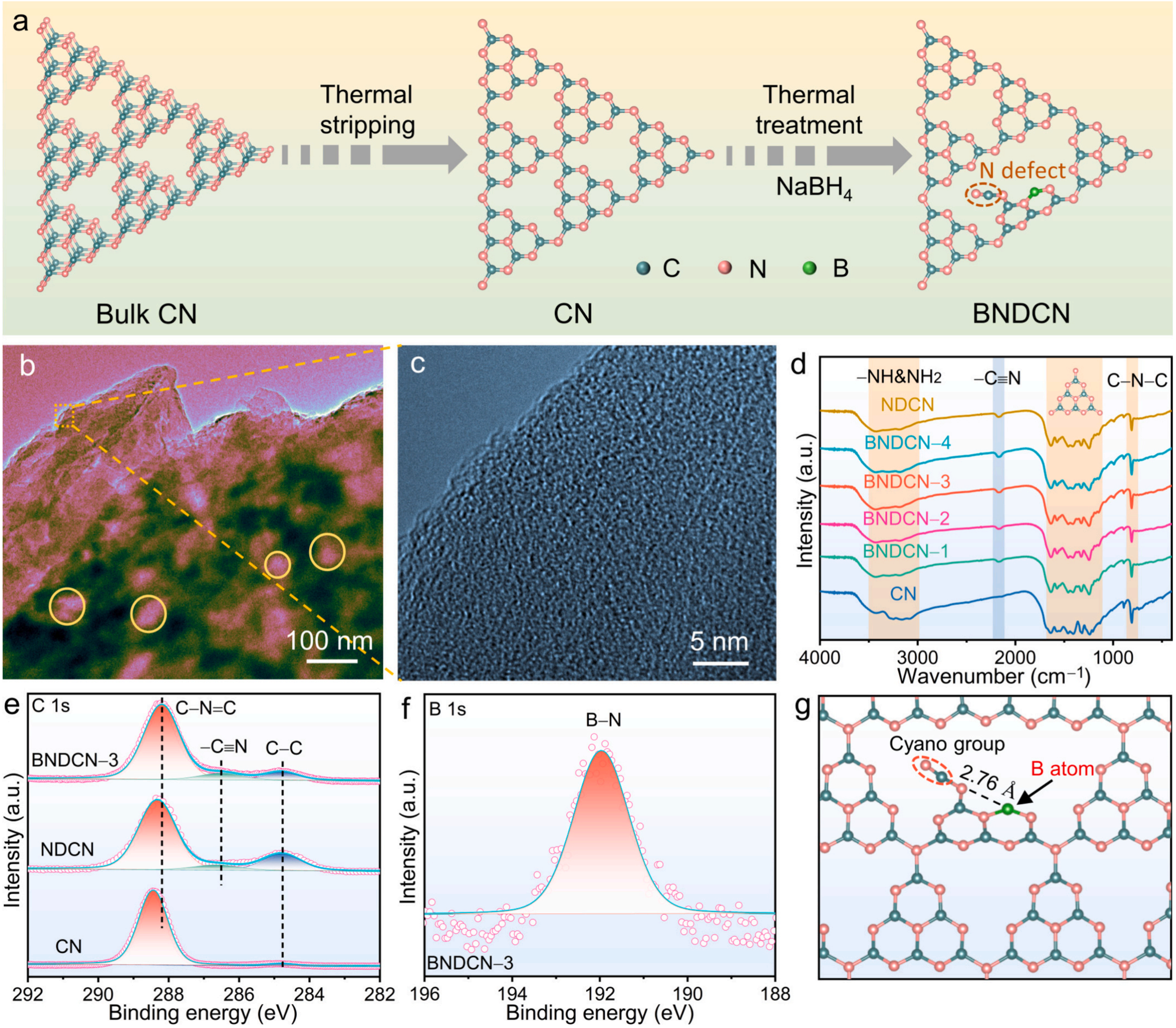

Fig. 1. (a) Schematic illustration of the synthetic process of the BNDCN catalyst. (b) TEM and (c) HRTEM images of the BNDCN–3. (d) FTIR spectra of as-prepared samples. The high-resolution XPS spectra of (e) C 1 s and (f) B 1 s for as-prepared samples. (g) The optimized structure of BNDCN model. The grass green, brick red, and green balls represent C, N, and B atoms, respectively. (For interpretation of the references to color in this figure legend, the reader is referred to the web version of this article.)

spectrum of BNDCN–3 shows a distinct peak at 191.97 eV, corresponding to B—N bonds (**Fig. 1**f) [32]. The Na 1 s XPS spectra of both the NDCN and BNDCN–3 samples exhibit a binding energy at 1070.96 eV, which may be attributed to physically adsorbed Na^+ ion (**Fig. S6**c) [33], while only a trace amount of Cl^- ion is detected in the NDCN sample (**Fig. S6**d, **Table S1**) [34]. Collectively, these results confirm the successful co-modification of the CN framework with B dopants and cyano group. This leads to the in situ formation of metal-free FLPs within the material (**Fig. 1**g).

3.2. In-depth exploration of the metal-free FLPs evolution mechanism

Accordingly, molecular orbital theory was employed to investigate the feasibility of forming metal-free FLP configurations [35]. The B atom has a fully occupied 2 s orbital containing two electrons with opposite spins, while the 2p orbital hosts a single unpaired electron and is divided into three suborbitals ($2p_x$, $2p_y$, and $2p_z$) (Figs. 2a and **S7**a). Upon excitation, the $2p_x$ and $2p_y$ suborbitals each accommodate one unpaired electron. Subsequently, the 2 s orbital hybridizes with the $2p_x$ and $2p_y$ suborbitals to generate three equivalent sp^2 hybrid orbitals, while the $2p_z$ suborbital remains unoccupied. Similarly, for the N atom, the ground-state electronic configuration consists of a fully occupied 2 s orbital and three 2p suborbitals ($2p_x$, $2p_y$, and $2p_z$) with the unpaired electron (Figs. 2a and **S7**b). Upon excitation, the $2p_x$ suborbital is occupied with paired electrons, while the $2p_y$ suborbital contains a single unpaired electron. Subsequent hybridization of the 2 s orbital and two suborbitals ($2p_x$ and $2p_y$) yields three nonequivalent sp^2 hybrid orbitals, whereas the $2p_z$ suborbital retains one unpaired electron. After hybridization of the C, N, and B atoms, their sp^2 hybrid orbitals overlap to form σ-bonds, while the overlap of their $2p_z$ suborbitals featuring the unpaired electron leads to the formation of π-bonds [35]. These characteristics render B and N atoms well-suited for constructing metal-free FLPs within the sp^2-hybridized π-conjugated CN framework. When the B atom substitutes for the C atom within the CN substrate, an adjacent

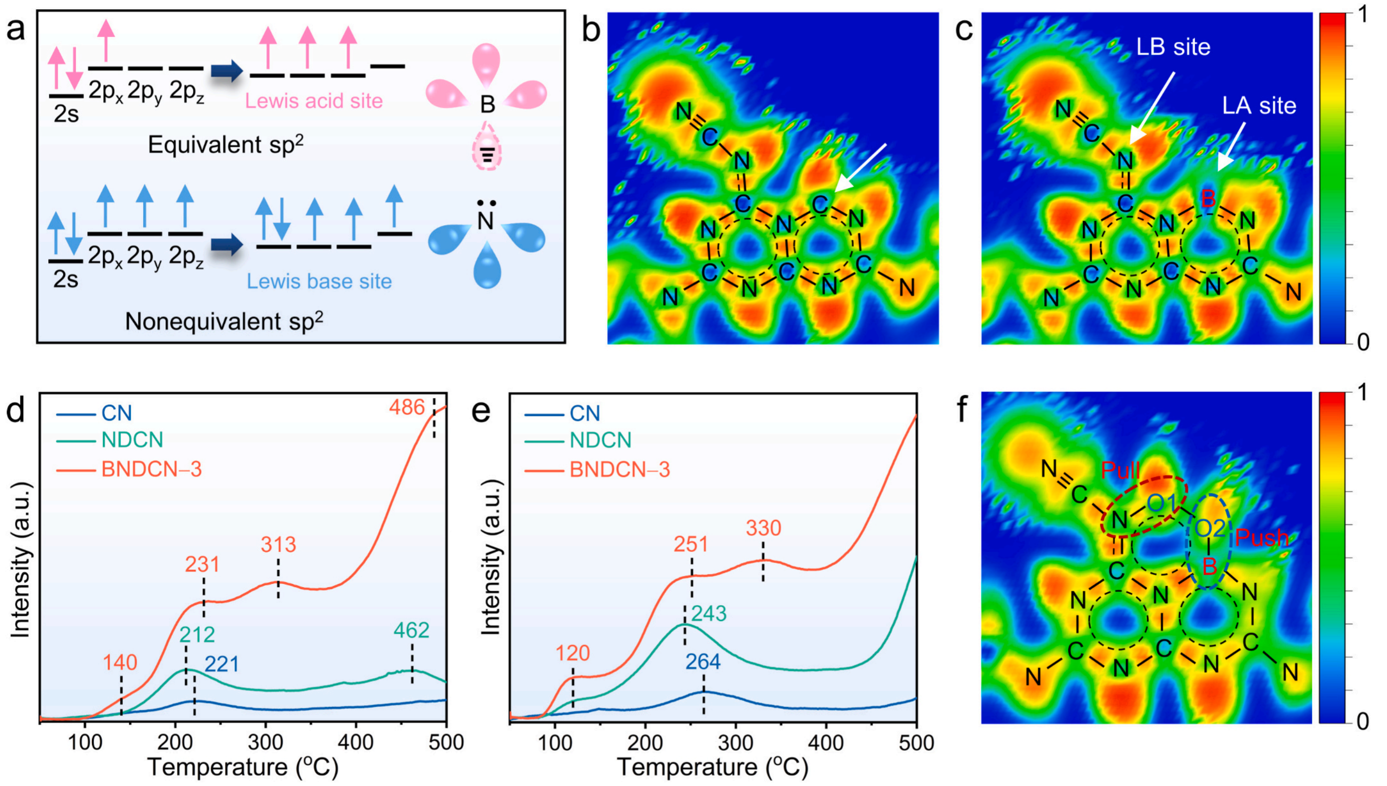

Fig. 2. (a) The equivalent sp^2 hybridization diagrams of the B atom and the nonequivalent sp^2 hybridization diagrams of the N atom. ELF contours of (b) NDCN and (c) BNDCN models. (d) CO_2-TPD, (e) NH_3-TPD profiles of as-prepared CN, NDCN, and BNDCN–3 samples. (f) ELF contour of O_2 adsorbed on the metal-free FLP sites within the BNDCN model. The blue and red regions were assigned to electron depletion and accumulation in Figures b-c and f. (For interpretation of the references to color in this figure legend, the reader is referred to the web version of this article.)

cyano group is simultaneously generated, resulting in the formation of metal-free FLPs between the doped B atoms and adjacent cyano-group N atoms. The charge density distribution was analyzed by electron localization function (ELF) contours. The symmetric electron distribution in tri-*s*-triazine (heptazine) reflects the π-conjugated configuration of CN model (**Fig. S8**) [36]. In contrast, the NDCN model exhibits enhanced electron density around the cyano group, the N atom adjacent to the cyano group, and the C atom (marked by a white arrow) (Fig. 2b and **S9**). Substituting the C atom with the B atom in the NDCN model to obtain optimized BNDCN model results in a spatial distance of 2.76 Å between the B atom and the N atom adjacent to the cyano group within the FLP configuration (Fig. 1g). Furthermore, the electron density becomes more concentrated on the N atom adjacent to the cyano group, while the B atom exhibits electron-deficient character. This redistribution confirms that the N atom near the cyano group can act as an electron donor (LB site), whereas the B atom functions as an electron acceptor (LA site), together constituting the metal-free FLP structure within the CN matrix (Figs. 1g and 2c).

Temperature-programmed desorption (TPD) of CO_2 and NH_3 was performed to verify the presence and density of FLPs in BNDCN [37]. In the CO_2-TPD profiles, CN exhibits two desorption peaks at 140 and 221 °C, corresponding to the weak basic sites (Fig. 2d). Upon introducing the cyano group into CN, a new desorption peak appears at 462 °C, which can be attributed to the formation of cyano group. Remarkably, the BNDCN–3 catalyst displays an additional desorption peak at 313 °C, accompanied by a shift of the high-temperature desorption peak to 486 °C, indicating the generation of stronger base sites. Moreover, the total CO_2 desorption intensity of BNDCN–3 is significantly higher than that of CN and NDCN, reflecting an increased amount of surface basicity. Similarly, NH_3-TPD analysis shows that BNDCN–3 exhibits markedly stronger and broader desorption peaks compared to the contrast samples, confirming the presence of abundant acidic sites (Fig. 2e). The concurrent enhancement in both CO_2- and NH_3-TPD profiles suggests the coexistence of numerous LA and LB sites, which is characteristic of customized metal-free FLPs in BNDCN. To further validate the nature of these LA sites, pyridine-FTIR spectra were recorded for BNDCN–3 (**Fig. S10**). A typical characteristic peak of LA sites at 1442 cm^{-1} was observed, while only a weak peak of Brønsted acid (BA) sites at 1551 cm^{-1} appeared, proving that the acidity predominantly arises from LA sites [38]. These results collectively demonstrate the successful construction of metal-free FLPs in BNDCN. The coexistence of these LA and LB sites enhances the surface polarization and facilitates charge separation, thereby promoting the interfacial O_2 activation and improving photocatalytic reduction performance [39]. The optimal O_2 adsorption configuration on the FLP sites is illustrated by ELF contours in Fig. 2f. The O atom **1** of the O_2 molecule accepts electrons from the LB site (a pull effect), while the O atom **2** donates electrons to the LA site (a push effect). This synergistic “push–pull” effect facilitates efficient O_2 adsorption within the stable six-membered heterocyclic configuration, promoting O_2 activation.

3.3. *Catalytic activity and selectivity of BNDCN for O_2PR*

The photocatalytic H_2O_2 evolution performance of the as-prepared samples was evaluated in a liquid-solid reaction system under ultraviolet-visible (UV–vis) light irradiation (320–780 nm) with continuous O_2 supply. The generated H_2O_2 contents were quantitatively determined using the iodometric spectrophotometric method (**Fig. S11**) [40]. As shown in Figs. 3a, **S12**, and **S13**, all as-prepared catalysts steadily evolve H_2O_2 production both in the presence and absence of the hole sacrificial agent. The photocatalytic activity of the BNDCN–X catalysts, where X varies from 1 to 4, follows a volcano-shaped trend (Figs. 3b and c). In the presence of the sacrificial agent, the optimized BNDCN–3 catalyst demonstrates the highest photocatalytic H_2O_2

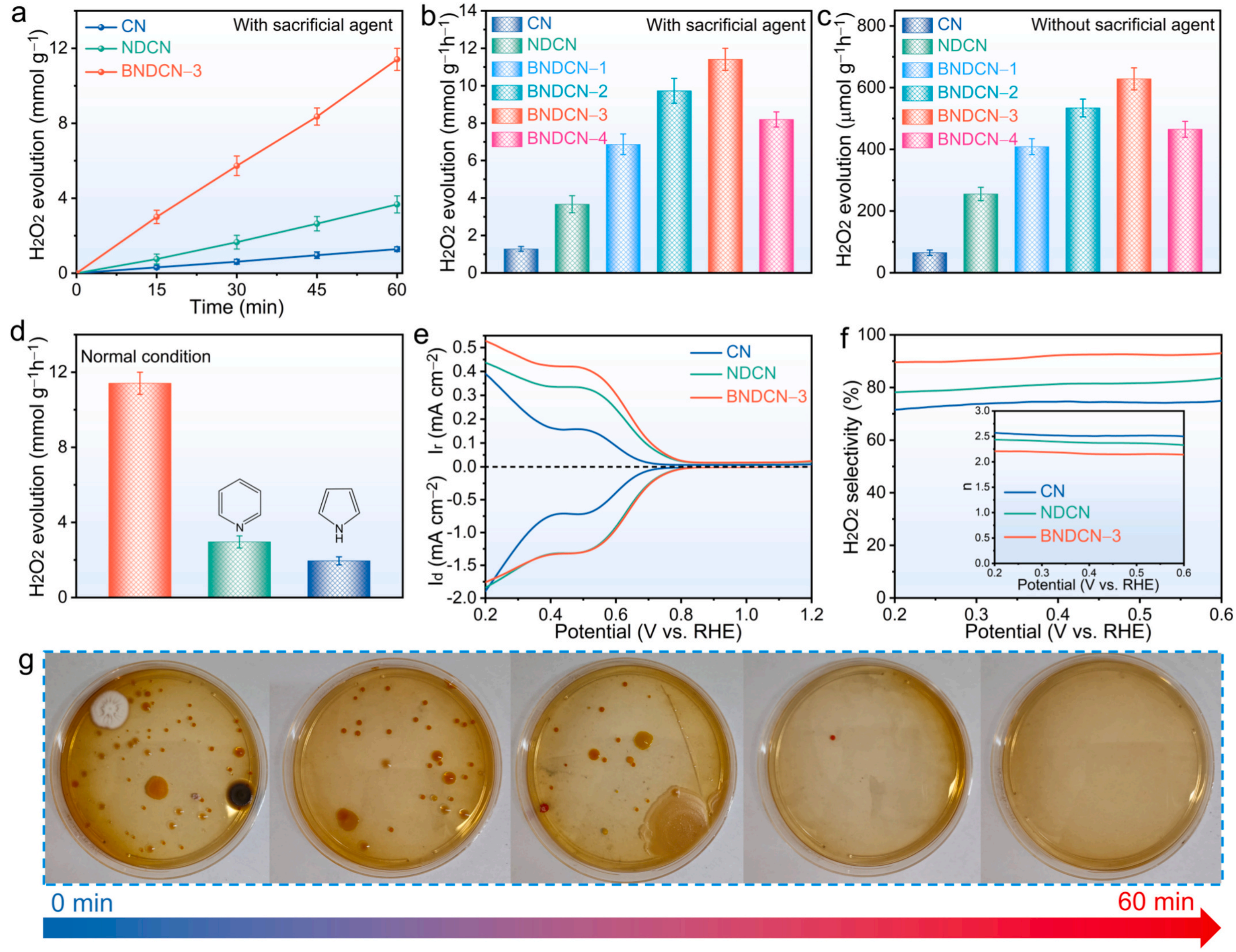

Fig. 3. (a) Typical time courses of H_2O_2 production on as-prepared catalysts. Average H_2O_2 evolution rates of the different catalysts in (b) a sacrificial agent and (c) pure-water system. (d) Influence of molecular LB or LA on the catalytic activity of the BNDCN–3 catalyst for photocatalytic H_2O_2 generation in the sacrificial agent system. Three repeated experiments were carried out for all the error estimates. (e) RRDE polarization curves over CN, NDCN, and BNDCN–3 samples in O_2-saturated 0.1 M KOH at 1600 rpm with ring current (upper part) and disk current (bottom part). (f) H_2O_2 selectivity as a function of the applied potential. The inset shows the calculated average number of transferred electrons (n). (g) Antibacterial experiments were conducted using reaction solutions collected at different photocatalytic reaction times to evaluate their effects on bacteria present in lake water.

evolution activity of 11.3 mmol g^{-1} h^{-1}, which is approximately 6.3 and 3.0 times higher than that of the CN (1.8 mmol g^{-1} h^{-1}) and NDCN (3.8 mmol g^{-1} h^{-1}), respectively (Fig. 3b). A similar activity trend is observed in the pure water system without a sacrificial agent (Figs. 3c and **S13**). Under these conditions, the BNDCN–3 catalyst achieves the highest H_2O_2 evolution rate of 628 μmol g^{-1} h^{-1}, which is approximately 9.7 and 2.5 times greater than that of CN (65 μmol g^{-1} h^{-1}) and NDCN (255 μmol g^{-1} h^{-1}), respectively (Fig. 3c). At 420 nm, the BNDCN–3 catalyst achieves an apparent quantum yield (AQY) of 13.1%, which is competitive with state-of-the-art CN-based photocatalysts for H_2O_2 production (**Fig. S14**, **Table S5**). The BNDCN–3 catalyst maintains nearly its original activity with minimal attenuation after five successive cycles, indicating exceptional photostability (**Fig. S15**). Furthermore, the morphology, crystal structure, molecular backbone configuration, elemental composition (except for physically adsorbed Na^+ ions), and chemical state of the hybrid are well preserved after five test cycles, reaffirming its excellent structural stability (**Figs. S16**, **S17**, and **Tables S6**, **S7**). The Na element in the BNDCN–3 sample decreases to about 0.1% after the photocatalytic cycling test (**Fig. S17**e, **Table S6**). These results demonstrate that the Na^+ ions are retained in BNDCN via physisorption. Control experiments reveal that no H_2O_2 is formed under dark conditions or with argon as reactant gas, validating that H_2O_2 originates exclusively from O_2 reactant gas under UV–vis light irradiation (**Fig. S18**). To elucidate the essential role of metal-free FLPs in the photocatalytic process, the photocatalytic reaction was carried out by introducing typical organic LB (pyridine) and LA (pyrrole) to occupy the LA and LB sites of the metal-free FLPs, respectively [37]. Moreover, control experiments were conducted to study the influence of organic pyridine and pyrrole. These results show that the addition of pyridine or pyrrole causes only negligible changes in the H_2O_2 evolution for the CN sample (**Fig. S19**a). The NDCN sample exhibits a similar trend upon addition of trace amounts of pyridine, while displaying slightly reduced performance upon addition of pyrrole (**Fig. S19**b). In contrast, a significant decrease in H_2O_2 yield is observed for the BNDCN–3 catalyst after the addition of these probe molecules (Fig. 3d). These results indicate that the suppression of H_2O_2 evolution mainly originates from the occupation of the FLP active sites rather than nonspecific adsorption of organic LB and LA. Therefore, these results unequivocally demonstrate that the metal-free FLP sites within the BNDCN play a pivotal role in facilitating O_2 activation and driving photocatalytic H_2O_2 evolution.

Photocatalytic selectivity is a critical factor in determining the overall H_2O_2 generation efficiency. To investigate how the metal-free FLPs in the CN substrate influence selective electron transfer during the oxygen reduction reaction (ORR), we performed electrochemical measurements using a rotating ring-disk electrode (RRDE) [41,42]. In this test, the disk current (I_d) and ring current (I_r) correspond to the ORR ($O_2 + 2H^+ + 2e^- \rightarrow H_2O_2$ or $O_2 + 4H^+ + 4e^- \rightarrow 2H_2O$) and the H_2O_2 oxidation reaction ($H_2O_2 \rightarrow O_2 + 2H^+ + 2e^-$), respectively. As shown in Fig. 3e (bottom), all samples exhibit a gradually increasing density of I_d as the potential decreased from 0.8 V (vs. reversible hydrogen electrode (RHE)). Notably, the BNDCN–3 catalyst possesses a significantly higher I_r than that of CN and NDCN (Fig. 3e, top), indicating enhanced H_2O_2 production via the $2e^-$ pathway. The H_2O_2 selectivity and the number of transferred electrons (n) were calculated in the potential range of 0.20–0.60 V (vs. RHE) (Fig. 3f). Compared to CN and NDCN, the BNDCN–3 catalyst exhibits significantly higher H_2O_2 selectivity and an average n closer to the theoretical value of 2, indicating a dominant $2e^-$ O_2 reduction pathway. Specially, at a potential of 0.40 V (vs. RHE), CN and NDCN show H_2O_2 selectivities of 74.7% and 81.4%, with corresponding n values of 2.50 and 2.38, respectively. In contrast, under the same conditions, the BNDCN–3 catalyst achieves a remarkable H_2O_2 selectivity of 92.6% with a corresponding n value of 2.14. Together with the photocatalytic performance results, these analyses confirm that the introduced metal-free FLPs effectively steer the reaction selectivity toward the $2e^-$ ORR pathway, thereby significantly enhancing the efficiency of H_2O_2 evolution.

3.4. Antibacterial experiments

The photocatalytic H_2O_2 solution was evaluated for practical applications. To eliminate the influence of the sacrificial agent on the bacteria, antibacterial experiments were performed using reaction solutions derived from a pure-water photocatalytic system. Photocatalytic solutions were collected at various time intervals (0, 15, 30, and 60 min) and mixed with lake water (**Table S8**). After 48 h of incubation in the dark, representative photographs of the sterilization results are shown in Fig. 3g, illustrating the antibacterial effects of the filtrates against microorganisms present in lake water. As expected, the sterilization efficiency increases progressively with higher H_2O_2 concentration. In contrast, negligible antibacterial activity was observed in the pure water control (**Fig. S20**). These results demonstrate that the photocatalytically generated H_2O_2 production exhibits pronounced bactericidal activity, highlighting its potential applications in biological fields.

3.5. In-depth exploration of the accurate ORR pathways

A major challenge in the field is the accurate elucidation of ORR pathways, hindered by the difficulty in detecting transient intermediates such as singlet oxygen ($^1O_2$). To probe the H_2O_2 formation mechanism in the synthesized photocatalysts, key reaction intermediates were detected via electron spin resonance (ESR) spectroscopy in the presence of a sacrificial agent. Specifically, the DMPO agent was used to trap superoxide radical ($\cdot O_2^-$) and ·OOH, while TEMP agent was used to trap $^1O_2$ signals [43–45]. ESR spectra confirm the coexistence of three crucial intermediates, including $\cdot O_2^-$, $^1O_2$, and ·OOH, implying four possible mechanisms of O_2PR into H_2O_2 (Fig. 4a). In this process, photogenerated electrons migrate to the catalyst surface and react with adsorbed O_2 molecules to yield these reactive species. As shown in Figs. 4b–d, the signal intensities of all three intermediates increase significantly upon cyano group modification of CN, demonstrating that the cyano group effectively facilitates charge separation and elevates the concentration of photogenerated electrons. Notably, the BNDCN–3 catalyst exhibits even stronger ESR signals than NDCN, indicating that the synergistic effects between B dopant and the electron-enriched nitrogen species within the metal-free FLPs further lower the charge-transfer barrier and accelerate the formation of reactive oxygen intermediates. To further unveil the dominant reaction pathways, quenching experiments were performed using TEMP and p-

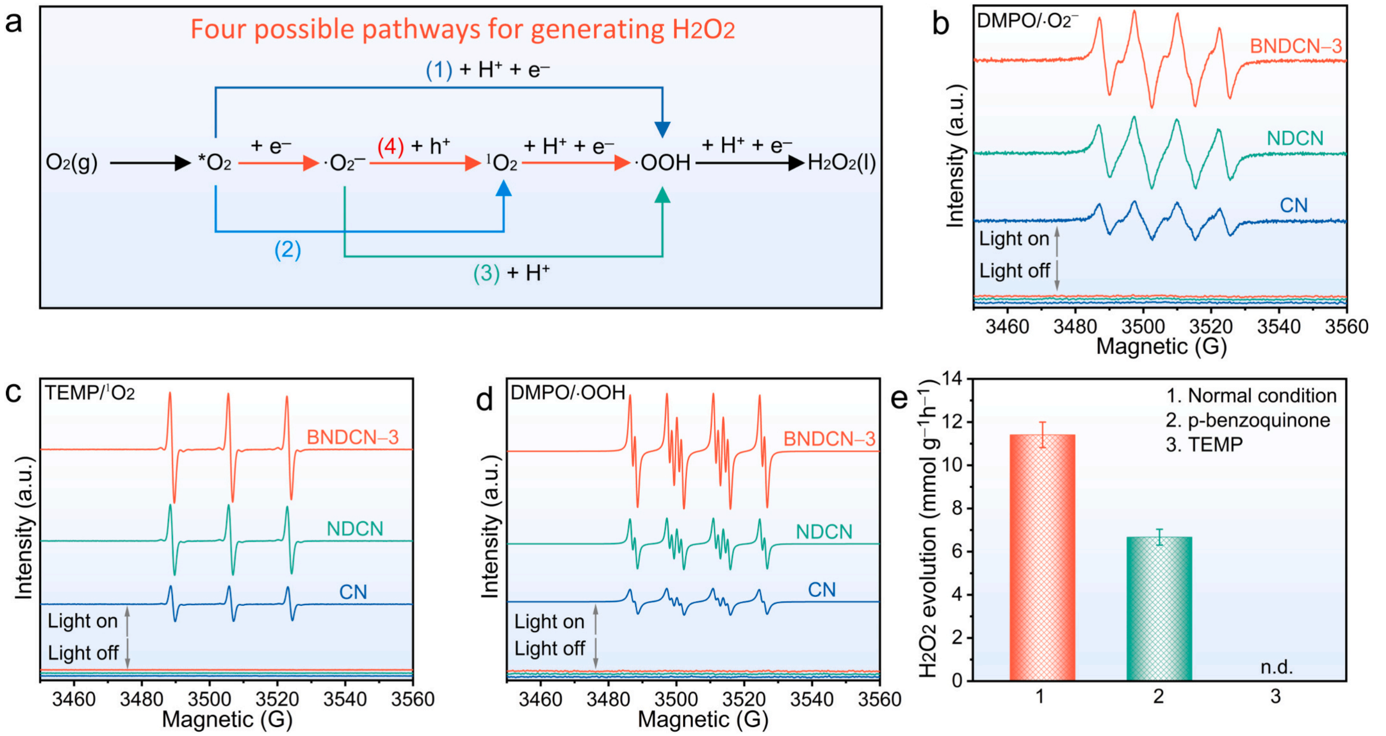

Fig. 4. (a) Schematics for the four possible mechanisms of the photocatalytic stoichiometric syntheses of H_2O_2 by the O_2 reduction reaction. (b) DMPO/$\cdot O_2^-$, (c) TEMP/$^1O_2$, and (d) DMPO/·OOH adducts formed in (b) methylbenzene, (c) aqueous suspension, and (d) methanol-water suspension of CN, NDCN, and BNDCN–3 samples over the dark and under 60 s of light irradiation. (e) H_2O_2 evolution rates over BNDCD–3 sample with or without the addition of p-benzoquinone and TEPM as $\cdot O_2^-$ and $^1O_2$ scavengers, respectively. Three repeated experiments were carried out for all the error estimates.

benzoquinone as $^1O_2$ and $\cdot O_2^-$ radical scavengers, respectively (Fig. 4e). The complete suppression of H_2O_2 formation upon TEMP addition indicates that photoinduced $^1O_2$ plays an indispensable role in the reaction, thereby excluding the pathways **(1)** and **(3)**. Furthermore, the pronounced decrease in H_2O_2 yield in the presence of p-benzoquinone demonstrates the key involvement of $\cdot O_2^-$ radicals in the photocatalytic reaction, suggesting the coexistence of reaction pathways **(2)** and **(4)**. Based on this, two dominant O_2 reduction reaction routes are proposed: a) $O_2 \rightarrow \cdot O_2^- \rightarrow {}^1O_2 \rightarrow \cdot OOH \rightarrow H_2O_2$; b) $O_2 \rightarrow {}^1O_2 \rightarrow \cdot OOH \rightarrow H_2O_2$.

3.6. *Electronic structure and carrier separation properties of BNDCN*

The enhanced photocatalytic activity and selectivity can be primarily attributed to three factors: 1) a modified electronic structure, 2) improved separation and transfer of photogenerated charge carriers, and 3) the favorable interfacial interaction of O_2 at the metal-free FLP sites [24]. The UV–vis diffuse reflectance spectra (DRS) of the as-obtained CN, NDCN, and BNDCN samples display broad absorption tails extending up to 800 nm, which are ascribed to the Urbach tail arising from midgap states located near the conduction band (E_{CB}) of defective CN (Figs. 5a and **S21**) [46]. Compared with CN, NDCN shows slightly enhanced Urbach tail absorption due to the introduction of the cyano group. Notably, the Urbach tail absorption of BNDCN increases significantly with increasing $NaBH_4$ dosage during thermal treatment, indicating an elevated density of metal-free FLPs. The corresponding Urbach energy (E_u) can be estimated by taking the inverse of the slope of the plots of the natural logarithm of the absorption coefficient against the photon energy (**Fig. S22**) [24]. The E_u values increase from 0.22 eV for CN to 0.55 eV for BNDCN–4 sample. Moreover, the intrinsic band gap of BNDCN is narrower than that of CN, extending their light absorption into the visible region (**Fig. S23**). Mott–Schottky (M–S) plots further reveal that CN, NDCN, and BNDCN samples display similar flat-band potentials (E_{fb}) and retain n-type semiconductor characteristics (**Fig. S24**) [47]. Given the minimal deviation between E_{CB} and E_{fb} ($E_{CB} \approx E_{fb}$) in n-type semiconductors [47], the valence band (E_{VB}) and midgap state can be calculated using the band gap, E_{CB}, and E_u. Notably, both E_{CB} and midgap states initially upshift from −1.10 and − 0.86 V for CN to −1.23 and − 1.10 V for NDCN, and subsequently downshift into −1.16 and − 0.61 V (vs. normal hydrogen electrode (NHE), pH = 7) for BNDCN–4, respectively (Figs. 5b and **S25**). This evolution suggests that the introduction of B dopant and cyano group facilitates electron excitation from E_{VB} to E_{CB} or midgap states, thereby enabling more efficient utilization of low-energy photons. Consequently, more photoexcited electrons can populate midgap states below the E_{CB} in BNDCN,

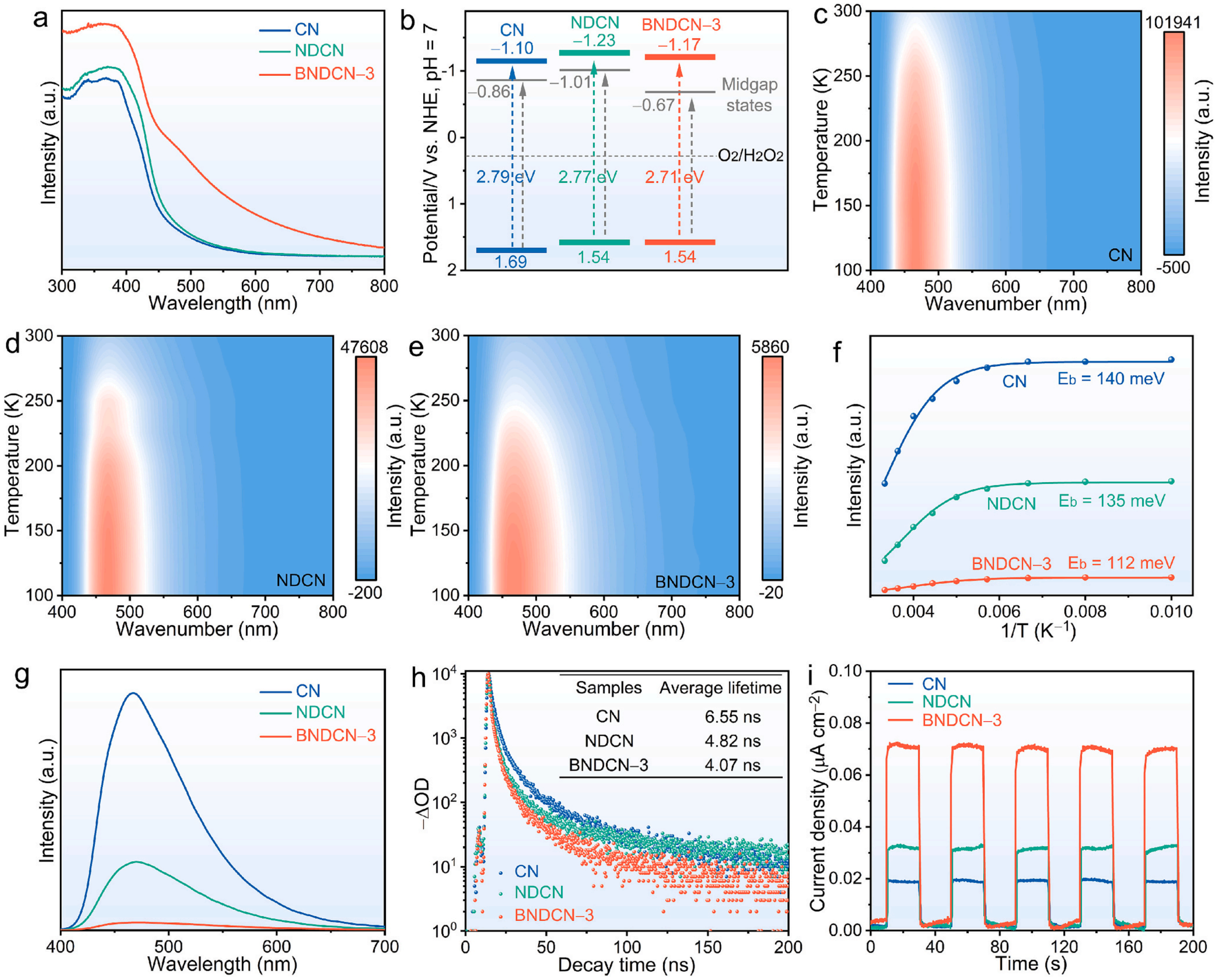

Fig. 5. (a) UV–vis DRS, and (b) electronic band structure with midgap states existing below the E_{CB} of CN, NDCN, and BNDCN–3 samples. The corresponding color contour map of TDPL over (d) CN, (e) NDCN, and (f) BNDCN–3 samples. (f) The integral of PL with different temperatures over the as-prepared samples. (g) PL, (h) TRPL, and (i) transient photocurrent of CN, NDCN, and BNDCN–3 samples under room temperature.

enhancing light-harvesting capacity and promoting charge transfer for efficient H_2O_2 photosynthesis.

The differences in electronegativity and electron affinity among B, C, and N atoms lead to uneven local electron densities upon incorporating B dopants and forming cyano groups into the CN framework [48]. These electronic modulations create a favorable environment for promoting photoexcited charge separation. To validate this hypothesis, the exciton binding energy (E_b), defined as the energy required to dissociate an electron–hole pair bound by the Coulomb force, serves as an effective indicator of photogenerated carrier separation efficiency. Temperature-dependent photoluminescence spectroscopy (TDPL) was conducted to determine E_b, and the normalized integrated PL intensities of the CN, NDCN, and BNDCN–3 samples were plotted as a function of temperature in the form of Arrhenius plots (**Figs. 5**c–e and **S26**). Accordingly, E_b can be calculated by the Arrhenius equation: [49].

$$I(T) = \frac{I_0}{1 + Ae^{-E_b/K_bT}} \tag{1}$$

where $I(T)$ is the normalized integrated PL intensity at temperature T, A is a constant related to the density of nonradiative recombination centers, and K_b is the Boltzmann constant.

Notably, the E_b of the BNDCN–3 sample is determined to be 112 meV, which is markedly lower than those of CN (140 meV) and NDCN (135 meV). This lower E_b underscores the superior ability of the metal-free FLPs to facilitate efficient charge carrier separation, directly contributing to the enhanced photoactivity (**Fig. 5**f). The reduced E_b of BNDCN–3 can be attributed to synergistic structural and electronic factors. Specifically, the surfaces of BNDCN–3 host abundant B dopant and adjacent cyano-group nitrogen arranged as metal-free FLP sites, resulting in a highly asymmetric local charge distribution and pronounced in-plane polarization [39]. This strong localized polarization facilitates the spatial separation of photoinduced electron-hole pairs, thereby suppressing their recombination. Upon photon absorption, the photoexcited electron can relax to the ground state via PL or transition to a non-emissive state through charge trapping, with a portion of these trapped charges subsequently participating in surface photochemical reactions [50]. To elucidate the charge-trapping behavior, steady-state PL spectroscopy under room temperature was employed. Among the different samples, the BNDCN–3 catalyst exhibits the weakest PL emission intensity, indicating a substantially suppressed electron–hole recombination due to the synergistic effects of B dopant and cyano group in the CN substrate (**Fig. 5**g) [51]. Furthermore, considering that BNDCN–3 sample also displays stronger light absorption than CN and NDCN, a larger proportion of their photoexcited states likely transition to non-emissive states, further facilitating charge separation (**Fig. 5**a). To further probe the charge carrier dynamics, time-resolved PL (TRPL) spectra under room temperature were analyzed using a biexponential decay model to estimate the average radiative lifetimes (**Fig. 5**h). The average lifetime of BNDCN–3 (4.07 ns) is significantly shorter than that of CN (6.55 ns) and NDCN (4.82 ns), indicating that the coexistence of B dopant and the electron-enriched nitrogen species within the metal-free FLPs promotes faster nonradiative decay and charge carrier transfer [52]. The increased nonradiative decay can be attributed to efficient photocarrier trapping by the metal-free FLPs, which favors subsequent surface catalytic reactions. Consistent with these results, BNDCN–3 exhibits the highest photocurrent density among as-prepared samples, demonstrating more efficient charge separation and migration under illumination (**Fig. 5**i). Moreover, the electrochemical impedance spectra (EIS) and the fitting results of EIS reveal that BNDCN–3 sample possesses the smallest semicircular arc radius in Nyquist plots and the lowest interfacial charge transfer resistance (R_{ct}) among as-prepared samples (**Fig. S27** and **Table S9**) [53]. Collectively, these results demonstrate that the engineered metal-free FLPs in BNDCN effectively enhance photocatalytic efficiency by boosting exciton dissociation and improving charge transport.

3.7. *In-depth exploration of catalytic enhancement mechanism*

In-situ diffuse reflectance infrared Fourier transform spectroscopy (DRIFTS) measurements were conducted to monitor the evolution of reaction intermediates during photocatalytic O_2 reduction. As displayed in **Figs. 6**a, b and **S28**a, light illumination over the CN sample induces the sequential formation and accumulation of several reactive intermediate species, including $\cdot O_2^-$ (1007, 1080, and 1144 cm^{-1}) [54–56], ·OOH (1214, 1274, and 1460 cm^{-1}) [54,57,58], adsorbed H_2O_2 ($*H_2O_2$, 1346, and 1431 cm^{-1}) [59,60]. Upon the incorporation of the cyano group, the NDCN exhibits intensified vibrational signals of O_2-derived intermediates compared to CN, which can be ascribed to the strengthened adsorption and activation of O_2 under light irradiation (**Figs. 6**c, d, and **S28**b). Significantly, these signal intensities of these characteristic peaks for BNDCN–3 further increase with prolonged light irradiation time, confirming the accelerated formation and stabilization of oxygenated intermediates (**Figs. 6**e, f, and **S28**c). These observations demonstrate the synergistic interaction between abundant B dopants and the electron-enriched nitrogen species within the metal-free FLPs, facilitating the injection of more photoinduced electrons into $*O_2$ molecules, thereby expediting the overall photocatalytic efficiency.

Density functional theory (DFT) calculations were performed to elucidate the intrinsic role of metal-free FLPs in the activation and reduction of O_2. The adsorption energy analysis reveals that the introduction of metal-free FLP active sites markedly lowers O_2 adsorption energy compared to the single active sites across the CN, NDCN, and BNDCN models (**Fig. 6**g). To further clarify the interfacial electron transfer, charge density differences after O_2 adsorption were calculated and analyzed. The Bader charge analysis indicates a progressive increase in charge transfer from the active sites to the adsorbed O_2 ($*O_2$) species, quantified as 0.041 |e| for CN, 0.638 |e| for NDCN, and then 0.873 |e| for BNDCN (**Figs. 6**h–j). These results clearly demonstrate that the presence of metal-free FLPs in BNDCN substantially strengthens O_2 adsorption and activation. The Gibbs free energy diagrams of O_2–to–H_2O_2 conversion involving various intermediates and corresponding energy barriers were investigated, revealing the impact of metal-free FLPs on BNDCN (**Figs. 6**k and **S29-S31**). All the models exhibit the same rate-determining step (RDS) related to the conversion of adsorbed O_2 to $*O_2$ species. NDCN featuring with cyano group displays a smaller energy barrier of RDS (3.41 eV) than that of CN (5.89 eV). Remarkably, the introduction of B dopant and adjacent cyano-group nitrogen to form metal-free FLPs further decreases the RDS barrier to 2.38 eV for BNDCN, accompanied by the lowest overall energy barrier for the protonation steps. This pronounced reduction in activation energy highlights that the synergistic interaction between B dopant and the electron-enriched nitrogen species within the FLPs effectively tailors the local electronic interactions, thereby accelerating the reaction kinetics of the $2e^-$ O_2PR pathway toward H_2O_2 formation.

4. Conclusion

In summary, this work demonstrates a feasible strategy for constructing atomically dispersed metal-free FLPs within BNDCN photocatalyst for efficient photocatalytic H_2O_2 generation. In previously reported studies [9,13,14], ORR at single metal active sites induces spatially asymmetric orbital coupling with O_2, confining charge transfer to a unidirectional pathway and potentially causing orbital decoupling of the O—O bond in $*O_2$ and ·OOH intermediates. In contrast, dual-metal sites often interact too strongly with O_2, excessively weakening or cleaving the O—O bond and thereby favoring the $4e^-$ reduction to H_2O over the selective $2e^-$ pathway to H_2O_2. Here, the electron-deficient B dopants and electron-rich N sites adjacent to cyano group synergistically create metal-free FLPs, enabling a "push–pull" electronic effect that enhances O_2 activation and charge transfer while suppressing O—O bond cleavage. The optimized BNDCN photocatalyst achieves a superior H_2O_2 evolution rate and remarkable stability. Furthermore, the

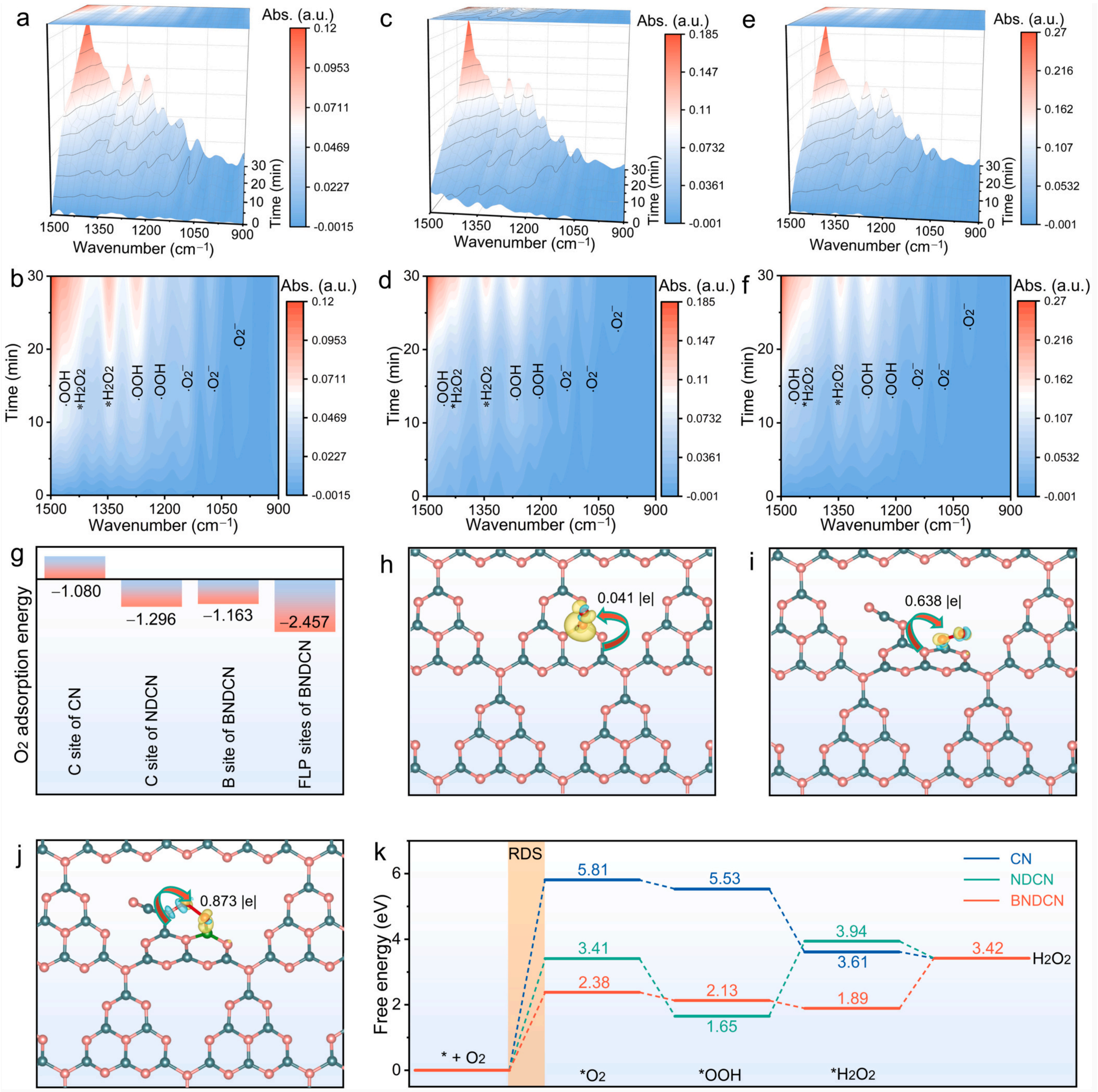

Fig. 6. (a, c, e) 3D color surface map and (b, d, f) the corresponding color contour map of in-situ DRIFTS of as-prepared samples exposed to a mixture gas of He, O_2, and H_2O with and without light irradiation: (a, b) CN, (c, d) NDCN, (e, f) BNDCN–3 samples. (g) Adsorption energy of O_2 on CN, NDCN, and BNDCN models. Charge density difference maps for $*O_2$ intermediate adsorption on the active site within (h) CN, (i) NDCN, and (j) BNDCN models. The isosurface value are set to 0.0005, 0.03, and 0.03 e Å^{-3}, respectively. The yellow and cyan regions represent charge accumulation and depletion upon $*O_2$ adsorption. (k) Gibbs free energy diagrams of O_2 reduction on CN, NDCN, and BNDCN models. The ball-and-stick models are also presented, in which the C, N, and B atoms are represented by grass green, brick red, and green balls, respectively.

resulting photocatalytic reaction solution shows significant sterilization efficacy. Comprehensive spectroscopic and theoretical analyses reveal that the metal-free FLPs significantly enhance exciton dissociation, interfacial charge transfer, and the selectivity of the $2e^-$ O_2PR pathway. This study not only deepens the understanding of metal-free FLP-induced photocatalytic mechanisms but also offers a general approach for designing high-efficiency, sustainable, and metal-free photocatalysts for solar-driven chemical transformations.

CRediT authorship contribution statement

Lei Li: Writing – original draft, Validation, Data curation, Conceptualization. **Hangjing Yu:** Writing – original draft, Validation, Data curation. **Kangjie Gao:** Validation, Formal analysis. **Linfeng Jin:** Writing – review & editing, Formal analysis, Data curation. **Jinyang Zhang:** Visualization, Software. **Wentao Wang:** Visualization, Validation, Software, Methodology. **Yong Hu:** Writing – review & editing, Supervision, Project administration, Funding acquisition, Conceptualization.

Declaration of competing interest

The authors declare that they have no known competing financial interests or personal relationships that could have appeared to influence the work reported in this paper.

Acknowledgements

We appreciate the financial support from the National Natural Science Foundation of China (22272150 and 52262031). This work is carried out at Shanxi Supercomputing Center of China, and the calculations are performed on TianHe-2.

Appendix A. Supplementary data

Supplementary data to this article can be found online at https://doi.org/10.1016/j.jcis.2026.140469.

Data availability

The authors do not have permission to share data.

References

[1] Y. Zhang, C. Pan, G. Bian, J. Xu, Y. Dong, Y. Zhang, Y. Lou, W. Liu, Y. Zhu, H_2O_2 generation from O_2 and H_2O on a near-infrared absorbing porphyrin supramolecular photocatalyst, Nat. Energy 8 (2023) 361–371, https://doi.org/10.1038/s41560-023-01218-7.

[2] S. Yan, Y. Li, X. Yang, X. Jia, J. Xu, H. Song, Photocatalytic H_2O_2 generation reaction with a benchmark rate at air-liquid-solid joint interfaces, Adv. Mater. 36 (2024) 2307967, https://doi.org/10.1002/adma.202307967.

[3] Y. Li, D. Luan, X.W. Lou, Engineering of single-atomic sites for electro- and photo-catalytic H_2O_2 production, Adv. Mater. 36 (2024) 2412386, https://doi.org/10.1002/adma.202412386.

[4] K. Meng, J. Zhang, B. Cheng, X. Ren, Z. Xia, F. Xu, L. Zhang, J. Yu, Plasmonic near-infrared-response S-scheme ZnO/$CuInS_2$ photocatalyst for H_2O_2 production coupled with glycerin oxidation, Adv. Mater. 36 (2024) 2406460, https://doi.org/10.1002/adma.202406460.

[5] L. Ma, L. Zhang, X. Zhou, J. Yang, D. Li, X. Zhao, Y. Su, Y. Chen, Z.H. Liu, R. Jiang, Revealing the electron transfer mechanism of defective carbon nitride during photocatalytic H_2O_2 production, Nano Res. 19 (2026) 94907870, https://doi.org/10.26599/NR.2025.94907870.

[6] X. Zhang, D. Gao, B. Zhu, B. Cheng, J. Yu, H. Yu, Enhancing photocatalytic H_2O_2 production with Au co-catalysts through electronic structure modification, Nat. Commun. 15 (2024) 3212, https://doi.org/10.1038/s41467-024-47624-7.

[7] J.L. Zhou, Y.F. Mu, M. Qiao, M.R. Zhang, S.X. Yuan, M. Zhang, T.B. Lu, Unlocking one-step two-electron oxygen reduction via metalloid boron-modified $Zn_3In_2S_6$ for efficient H_2O_2 photosynthesis, Angew. Chem. Int. Ed. 64 (2025) e202506963, https://doi.org/10.1002/anie.202506963.

[8] D. Jiao, C. Ding, M. Xu, X. Ruan, S.K. Ravi, X. Cui, Modulating Yeager adsorption configuration of O_2 through cd doping in $Zn_3In_2S_6$ for photosynthesis of H_2O_2, Adv. Funct. Mater. 35 (2025) 2416753, https://doi.org/10.1002/adfm.202416753.

[9] X. Zhou, K. Cao, S. Huang, H. Wu, Z. Cao, H. Liu, P. Chen, D. Su, G. Wang, T. Wang, C. Wang, H. Pang, Synergistic conversion of hydrogen peroxide and benzaldehyde in air by silver single-atom modified thiophene-functionalized g-C_3N_4, Angew. Chem. Int. Ed. 64 (2025) e202505532, https://doi.org/10.1002/anie.202505532.

[10] B. Liu, J. Du, G. Ke, B. Jia, Y. Huang, H. He, Y. Zhou, Z. Zou, Boosting O_2 reduction and H_2O dehydrogenation kinetics: surface n-hydroxymethylation of g-C_3N_4 photocatalysts for the efficient production of H_2O_2, Adv. Funct. Mater. 32 (2022) 2111125, https://doi.org/10.1002/adfm.202111125.

[11] Q. Zhang, B. Wang, H. Miao, J. Fan, T. Sun, E. Liu, Efficient photocatalytic H_2O_2 production over K^+−intercalated crystalline g-C_3N_4 with regulated oxygen reduction pathway, Chem. Eng. J. 482 (2024) 148844, https://doi.org/10.1016/j.cej.2024.148844.

[12] Q. Zhang, H. Miao, J. Wang, T. Sun, E. Liu, Self-assembled S-scheme $In_{2.77}S_4$/K^+-doped g-C_3N_4 photocatalyst with selective O_2 reduction pathway for efficient H_2O_2 production using water and air, Chin. J. Catal. 63 (2024) 176–189, https://doi.org/10.1016/S1872-2067(24)60077-X.

[13] C. He, C.H. Lee, L. Meng, H.Y.T. Chen, Z. Li, Selective orbital coupling: an adsorption mechanism in single-atom catalysis, J. Am. Chem. Soc. 146 (2024) 12395–12400, https://doi.org/10.1021/jacs.3c13119.

[14] L. Xie, P. Wang, Y. Li, D. Zhang, D. Shang, W. Zheng, Y. Xia, S. Zhan, W. Hu, Pauling-type adsorption of O_2 induced electrocatalytic singlet oxygen production on N–CuO for organic pollutants degradation, Nat. Commun. 13 (2022) 5560, https://doi.org/10.1038/s41467-022-33149-4.

[15] Y. Zhao, K. Gao, J. Li, H. Liu, F. Chen, W. Wang, Y. Zhong, Y. Hu, Engineering of Lewis acid–base interfaces in Cu_2S/$ZnIn_2S_4$ hollow hetero-nanocages for enhanced photocatalytic CO_2 reduction, Nanoscale Horiz. 13 (2025) 2024–2054, https://doi.org/10.1039/D5NH00355E.

[16] Y. Shang, M. Zheng, H. Liu, X. Jin, C. Yan, L. Song, Z. Qi, F. Jing, P. Song, X. Zhou, G. Chen, C. Lv, Mimicking frustrated Lewis pairs on graphitic carbon nitride for CO_2 photoreduction, ACS Catal. 13 (2023) 14530–14539, https://doi.org/10.1021/acscatal.3c03628.

[17] L. Yu, Q. Wang, C. Zhuang, J.D. Huang, Y. Zhu, X. Jing, Y. Guo, Y.X. Tong, Z. Zhang, Periodic frustrated Lewis pairs on bimetallic oxide semiconductors for CO_2 adsorption and photocatalytic conversion, ACS Nano 19 (2025) 7239–7252, https://doi.org/10.1021/acsnano.4c17231.

[18] S. Zhang, Z.Q. Huang, Y. Ma, W. Gao, J. Li, F. Cao, L. Li, C.R. Chang, Y. Qu, Solid frustrated-Lewis-pair catalysts constructed by regulations on surface defects of porous nanorods of CeO_2, Nat. Commun. 8 (2017) 15266, https://doi.org/10.1038/ncomms15266.

[19] P. Zhu, X. Xiong, D. Wang, Y. Li, Advances and regulation strategies of the active moiety in dual-atom site catalysts for efficient electrocatalysis, Adv. Energy Mater. 13 (2023) 2300884, https://doi.org/10.1002/aenm.202300884.

[20] S. Huang, Z. Qiao, P. Sun, K. Qiao, K. Pei, L. Yang, H. Xu, S. Wang, Y. Huang, Y. Yan, D. Cao, The strain induced synergistic catalysis of FeN_4 and MnN_3 dual-site catalysts for oxygen reduction in proton- /anion- exchange membrane fuel cells, Appl. Catal. B-Environ. 317 (2022) 121770, https://doi.org/10.1016/j.apcatb.2022.121770.

[21] S. Ajmal, A. Rasheed, N.Q. Tran, X. Shao, Y. Hwang, V.Q. Bui, Y.D. Kim, J. Kim, H. Lee, Electron deficient boron-doped amorphous carbon nitride to uphill N_2 photo-fixation through π back donation, Appl. Catal. B-Environ. 321 (2023) 122070, https://doi.org/10.1016/j.apcatb.2022.122070.

[22] W. Lin, H. Chen, G. Lin, S. Yao, Z. Zhang, J. Qi, M. Jing, W. Song, J. Li, X. Liu, J. Fu, S. Dai, Creating frustrated Lewis pairs in defective boron carbon nitride for electrocatalytic nitrogen reduction to ammonia, Angew. Chem. Int. Ed. 61 (2022) e202207807, https://doi.org/10.1002/anie.202207807.

[23] D. Zhao, Y. Wang, C.L. Dong, Y.C. Huang, J. Chen, F. Xue, S. Shen, L. Guo, Boron-doped nitrogen-deficient carbon nitride-based z-scheme heterostructures for photocatalytic overall water splitting, Nat. Energy 6 (2021) 388–397, https://doi.org/10.1038/s41560-021-00795-9.

[24] L. Li, H. Liu, C. Cheng, X. Dai, F. Chen, J. Ning, W. Wang, Y. Hu, Photochemical tuning of tricoordinated nitrogen deficiency in carbon nitride to create delocalized π electron clouds for efficient CO_2 photoreduction, ACS Catal. 14 (2024) 10204–10213, https://doi.org/10.1021/acscatal.4c01636.

[25] L. Ma, J. Yang, P. Yang, L. Huang, X. Zhou, X. Zhao, J. Kang, Y. Fang, R. Jiang, Fragmented polymetric carbon nitride with rich defects for boosting electrochemical synthesis of hydrogen peroxide in alkaline and neutral media, ChemSusChem 18 (2025) e202401121, https://doi.org/10.1002/cssc.202401121.

[26] J. Li, X. Wang, L. Huang, L. Tian, M. Shalom, C. Xiong, H. Zhang, Q. Jia, S. Zhang, F. Liang, Ultrathin mesoporous graphitic carbon nitride nanosheets with functional cyano group decoration and nitrogen-vacancy defects for an efficient selective CO_2 photoreduction, Nanoscale 13 (2021) 12634–12641, https://doi.org/10.1039/D1NR02639A.

[27] L. Li, X. Dai, K. Gao, H. Yu, F. Chen, W. Wang, J. Ning, Y. Hu, Customized interfacial electronic interactions in protonated g-C_3N_4/$ZnIn_2S_4$ S-scheme 2D/2D edge-to-face heterostructures for boosted CO_2 photoconversion, Chem. Eng. J. 514 (2025) 163193, https://doi.org/10.1016/j.cej.2025.163193.

[28] X. Zhang, P. Ma, C. Wang, L. Gan, X. Chen, P. Zhang, Y. Wang, H. Li, L. Wang, X. Zhou, K. Zheng, Unraveling the dual defect sites in graphite carbon nitride for ultra-high photocatalytic H_2O_2 evolution, Energy Environ. Sci. 15 (2022) 830–842, https://doi.org/10.1039/d1ee02369a.

[29] L. Li, X. Dai, C. Cheng, F. Chen, S.M. Wabaidur, W. Wang, Y. Hu, Synergy of Ni single atoms and NiO nanoclusters in carbon nitride to create local charge polarization for enhanced CO_2 photoreduction, Chem. Eng. J. 507 (2025) 160101, https://doi.org/10.1016/j.cej.2025.160101.

[30] Y. Xiao, G. Tian, W. Li, Y. Xie, B. Jiang, C. Tian, D. Zhao, H. Fu, Molecule self-assembly synthesis of porous few-layer carbon nitride for highly efficient photoredox catalysis, J. Am. Chem. Soc. 141 (2019) 2508–2515, https://doi.org/10.1021/jacs.8b12428.

[31] E. Wierzyńska, K. Korytkowska, K. Kazimierczuk, T. Łęcki, K. Zarębska, K. P. Korona, M. Pisarek, B. Furtak, M. Skompska, The role of boron dopant in the improvement of electron transfer in g-C_3N_4 photocatalyst, J. Phys. Chem. C 128 (2024) 894–907, https://doi.org/10.1021/acs.jpcc.3c06373.

[32] F. Gao, H. Xiao, J. Yang, X. Luan, D. Fang, L. Yang, J. Zi, Z. Lian, Modulation of electronic density in ultrathin g-C_3N_4 for enhanced photocatalytic hydrogen evolution through an efficient hydrogen spillover pathway, Appl. Catal. B-Environ. 341 (2024) 123334, https://doi.org/10.1016/j.apcatb.2023.123334.

[33] P. Yadav, A. Sharma, U.K. Goutam, I. Bhaumik, G. Singh, Elucidation of amphoteric nature of Pr_2O_3 using XPS and conductivity measurement in lead-free NKBT host lattice, J. Alloys Compd. 1006 (2024) 176189, https://doi.org/10.1016/j.jallcom.2024.176189.

[34] Y. Zhang, Z. Xu, Q. Wang, W. Hao, X. Zhai, X. Fei, X. Huang, Y. Bi, Unveiling the activity origin of ultrathin BiOCl nanosheets for photocatalytic CO_2 reduction, Appl. Catal. B-Environ. 299 (2021) 120679, https://doi.org/10.1016/j.apcatb.2021.120679.

[35] L. Ma, Y. Gao, B. Wei, L. Huang, N. Zhang, Q. Weng, L. Zhang, S.F. Liu, R. Jiang, Visible-light photocatalytic H_2O_2 production boosted by frustrated Lewis pairs in defected polymeric carbon nitride nanosheets, ACS Catal. 14 (2024) 2775–2786, https://doi.org/10.1021/acscatal.3c05360.

[36] P. Xia, B. Cheng, J. Jiang, H. Tang, Localized π-conjugated structure and EPR investigation of g-C_3N_4 photocatalyst, Appl. Surf. Sci. 487 (2019) 335–342, https://doi.org/10.1016/j.apsusc.2019.05.064.

[37] B. Xu, S. Luo, W. Hua, H. Xiao, B. Chong, G. Yan, H. Li, H. Ou, B. Lin, G. Yang, Constructing atomic tungsten-based solid frustrated-Lewis-pair sites with d-p

interactions for selective CO_2 photoreduction, J. Am. Chem. Soc. 147 (2025) 200–210, https://doi.org/10.1021/jacs.4c08953.

[38] Y. Liu, H. Yang, F. Jin, Y. Zhang, Y. Li, Synthesis of pyridine and picolines over co-modified HZSM-5 catalyst, Chem. Eng. J. 136 (2008) 282–287, https://doi.org/10.1016/j.cej.2007.03.073.

[39] M. Zhou, H. Wang, R. Liu, Z. Liu, X. Xiao, W. Li, C. Gao, Z. Lu, Z. Jiang, W. Shi, Y. Xiong, Construction of frustrated Lewis pairs in poly(heptazine imide) nanosheets via hydrogen bonds for boosting CO_2 photoreduction, Angew. Chem. Int. Ed. 63 (2024) e202407468, https://doi.org/10.1002/anie.202407468.

[40] R. Du, K. Xiao, B. Li, X. Han, C. Zhang, X. Wang, Y. Zuo, P. Guardia, J. Li, J. Chen, J. Arbiol, A. Cabot, Controlled oxygen doping in highly dispersed Ni-loaded g-C_3N_4 nanotubes for efficient photocatalytic H_2O_2 production, Chem. Eng. J. 441 (2022) 135999, https://doi.org/10.1016/j.cej.2022.135999.

[41] J. Hou, K. Wang, X. Zhang, Y. Wang, H. Su, C. Yang, X. Zhou, W. Liu, H. Hu, J. Wang, C. Li, P. Ma, R. Zhang, Z. Wei, Z. Sun, Q. Liu, K. Zheng, Synergistic defect sites and CoO_x nanoclusters in polymeric carbon nitride for enhanced photocatalytic H_2O_2 production, ACS Catal. 14 (2024) 10893–10903, https://doi.org/10.1021/acscatal.4c00334.

[42] Z. Yuan, B. Li, Z. Wang, S. Lv, D. Zhang, H. Hou, W. Yang, H. Yang, X. Zhan, Frustrated Lewis pair–cyano dual-mediated ternary crystalline carbon nitride homojunctions for highly enhanced visible-light-driven photocatalytic H_2O_2 production, J. Mater. Chem. A 13 (2025) 36527–36539, https://doi.org/10.1039/D5TA06895A.

[43] L. Li, C. Guo, T. Li, C. Yang, F. Chen, W. Wang, R. Yan, J. Ning, Y. Hu, Ascorbic-acid-assisted in-situ construction of S-scheme CuO/Cu_2O hetero-nanosheets with active Cu(II)-O-Cu(I) bridges for efficient CO_2 photoreduction, Appl. Surf. Sci. 651 (2024) 159220, https://doi.org/10.1016/j.apsusc.2023.159220.

[44] X. Gao, H. Wei, W. Ma, W. Wu, W. Ji, J. Mao, P. Yu, L. Mao, Inflammation-free electrochemical in vivo sensing of dopamine with atomic-level engineered antioxidative single-atom catalyst, Nat. Commun. 15 (2024) 7915, https://doi.org/10.1038/s41467-024-52279-5.

[45] C. Zhao, X. Wang, Y. Yin, W. Tian, G. Zeng, H. Li, S. Ye, L. Wu, J. Liu, Molecular level modulation of anthraquinone-containing resorcinol-formaldehyde resin photocatalysts for H_2O_2 production with exceeding 1.2% efficiency, Angew. Chem. Int. Ed. 62 (2023) e202218318, https://doi.org/10.1002/anie.202218318.

[46] W. Tu, Y. Xu, J. Wang, B. Zhang, T. Zhou, S. Yin, S. Wu, C. Li, Y. Huang, Y. Zhou, Z. Zou, J. Robertson, M. Kraft, R. Xu, Investigating the role of tunable nitrogen vacancies in graphitic carbon nitride nanosheets for efficient visible-light-driven H_2 evolution and CO_2 reduction, ACS Sustain. Chem. Eng. 5 (2017) 7260–7268, https://doi.org/10.1021/acssuschemeng.7b01477.

[47] M. Ni, Y. Zhu, C. Guo, D.L. Chen, J. Ning, Y. Zhong, Y. Hu, Efficient visible-light-driven CO_2 methanation with self-regenerated oxygen vacancies in Co_3O_4/$NiCo_2O_4$ hetero-nanocages: vacancy-mediated selective photocatalysis, ACS Catal. 55 (2023) 2502–2512, https://doi.org/10.1021/acscatal.2c05577.

[48] P.K. Chattaraj, S. Duley, Electron affinity, electronegativity, and electrophilicity of atoms and ions, J. Chem. Eng. Data 55 (2010) 1882–1886, https://doi.org/10.1021/je900892p.

[49] H. Tan, W. Si, W. Peng, X. Chen, X. Liu, Y. You, L. Wang, F. Hou, J. Liang, Flexo−/piezoelectric polarization boosting exciton dissociation in curved two-dimensional carbon nitride photocatalyst, Nano Lett. 23 (2023) 10571–10578, https://doi.org/10.1021/acs.nanolett.3c03466.

[50] Y. Li, S. Zhang, C. He, H. Yao, C. Guo, W. Wang, Y. Hu, Modulation of Schottky barrier height and electronic structure in transition-metal@nitrogen-doped-carbon core–shell cocatalysts loaded with $Mn_xCd_{1-x}S$ nanorods for enhanced photocatalytic hydrogen evolution, ACS Catal. 15 (2025) 2315–2327, https://doi.org/10.1021/acscatal.4c06476.

[51] L. Li, X. Dai, D.L. Chen, Y. Zeng, Y. Hu, X.W. Lou, Steering catalytic activity and selectivity of CO_2 photoreduction to syngas with hydroxy-rich Cu_2S@R_{OH}-$NiCo_2O_3$ double-shelled nanoboxes, Angew. Chem. Int. Ed. 61 (2022) e202205839, https://doi.org/10.1002/anie.202205839.

[52] X. Zhang, H. Su, P. Cui, Y. Cao, Z. Teng, Q. Zhang, Y. Wang, Y. Feng, R. Feng, J. Hou, X. Zhou, P. Ma, H. Hu, K. Wang, C. Wang, L. Gan, Y. Zhao, Q. Liu, T. Zhang, K. Zheng, Developing Ni single-atom sites in carbon nitride for efficient photocatalytic H_2O_2 production, Nat. Commun. 14 (2023) 7115, https://doi.org/10.1038/s41467-023-42887-y.

[53] C. Wang, T. Xu, K. Gao, L. Jin, C. Guo, W. Wang, Y. Hu, Carbon doping synergistically regulates carrier separation kinetics and elementary reaction thermodynamics for efficient CO_2 photoreduction on Zn-polar ZnO nanocobbles, Appl. Catal. B-Environ. Energy 383 (2026) 126025, https://doi.org/10.1016/j.apcatb.2025.126025.

[54] Z. Gao, F. Liu, Z. Chen, Q. Song, P.J. Cullen, X. Zhang, Z. Zuo, J. Zhong, X. Lu, Z. Hu, R. Liu, Q. Zhang, Y. Yin, Y. Cai, Defect-modulated oxygen adsorption and Z-scheme charge transfer for highly selective H_2O_2 photosynthesis in pure water, Nat. Commun. 16 (2025) 8889, https://doi.org/10.1038/s41467-025-64166-8.

[55] Y. Chen, R. Liu, Y. Guo, G. Wu, T.C. Sum, S.W. Yang, D. Jiang, Hierarchical assembly of donor–acceptor covalent organic frameworks for photosynthesis of hydrogen peroxide from water and air, Nat. Synth. 3 (2024) 998–1010, https://doi.org/10.1038/s44160-024-00542-4.

[56] F. Chen, X. Lv, H. Wang, F. Wen, L. Qu, G. Zheng, Q. Han, Weak-field electro-flash induced asymmetric catalytic sites toward efficient solar hydrogen peroxide production, JACS Au 4 (2024) 1219–1228, https://doi.org/10.1021/jacsau.4c00076.

[57] S. Nayak, I.J. McPherson, K.A. Vincent, Adsorbed intermediates in oxygen reduction on platinum nanoparticles observed by in-situ IR spectroscopy, Angew. Chem. Int. Ed. 57 (2018) 12855–12858, https://doi.org/10.1002/anie.201804978.

[58] Y. Chen, T. Yang, Y. Jin, J. Li, J. Gu, X. Sun, Y. Zou, R. Liu, G. Wei, C. Yu, A. Kong, Chelated linkage and framework isomerism effect toward robust zn-salen MCOFs for dual-channel overall H_2O_2 photosynthesis, Adv. Funct. Mater. 35 (2025) 2508520, https://doi.org/10.1002/adfm.202508520.

[59] J. Hu, B. Li, X. Li, T. Yang, X. Yang, J. Qu, Y. Cai, H. Yang, Z. Lin, Lattice match-enabled covalent heterointerfaces with built-in electric field for efficient hydrogen peroxide photosynthesis, Adv. Mater. 36 (2024) 2412070, https://doi.org/10.1002/adma.202412070.

[60] H. Yan, J. Jiang, Y. Huang, M. Shen, J. Xu, Y.X. Ye, G. Ouyang, Inter-ring bonding electron donor structure triggers efficient two-electron water oxidation for photocatalytic hydrogen peroxide synthesis, Adv. Mater. 38 (2025) e07961, https://doi.org/10.1002/adma.202507961.